

Ultrafast shape change and joining of small-volume materials using nanoscale electrical discharge

Cheng-Cai Wang^{1,5}, Qing-Jie Li^{1,4}, Liang Chen^{1,2}, Yong-Hong Cheng², Jun Sun¹, Zhi-Wei Shan¹ (✉), Ju Li^{1,3} (✉), and Evan Ma^{1,4} (✉)

¹ Center for Advancing Materials Performance from the Nanoscale (CAMP-Nano) & Hysitron Applied Research Center in China (HARCC), State Key Laboratory for Mechanical Behavior of Materials, Xi'an Jiaotong University, Xi'an 710049, China

² State Key Laboratory of Electrical Insulation and Power Equipment, Xi'an Jiaotong University, Xi'an 710049, China

³ Department of Nuclear Science and Engineering and Department of Materials Science and Engineering, Massachusetts Institute of Technology, 77 Massachusetts Avenue, Cambridge, Massachusetts 02139, USA

⁴ Department of Materials Science and Engineering, Johns Hopkins University, Baltimore, Maryland 21218, USA

⁵ SJS Limited, 101 Xihuan Road, Jingzhou, Hubei 434024, China

Received: 29 September 2014

Revised: 30 November 2014

Accepted: 7 December 2014

© Tsinghua University Press and Springer-Verlag Berlin Heidelberg 2015

KEYWORDS

electrical discharge, welding, nanoscale, metallic glass, metal

ABSTRACT

Using nanoscale electrical-discharge-induced rapid Joule heating, we developed a method for ultrafast shape change and joining of small-volume materials. Shape change is dominated by surface-tension-driven convection in the transient liquid melt, giving an extremely high strain rate of $\sim 10^6 \text{ s}^{-1}$. In addition, the heat can be dissipated in small volumes within a few microseconds through thermal conduction, quenching the melt back to the solid state with cooling rates up to $10^8 \text{ K}\cdot\text{s}^{-1}$. We demonstrate that this approach can be utilized for the ultrafast welding of small-volume crystalline Mo (a refractory metal) and amorphous $\text{Cu}_{49}\text{Zr}_{51}$ without introducing obvious microstructural changes, distinguishing the process from bulk welding.

1 Introduction

Driven by the miniaturization trend in devices, interest in the mechanical properties of materials at micro- and nano-scales has grown worldwide [1–3]. It has been experimentally established that materials in this size-range exhibit extraordinary mechanical behaviors

compared to their bulk counterparts [4–8]. For example, it has been found that submicron-sized metallic glasses (MGs) exhibit unique mechanical properties compared to bulk samples, including unprecedented elastic strain (4%–5%) [5, 9] and tensile ductility [7, 8, 10]. In addition, plastic molding in the supercooled liquid state above the glass transition temperature, T_g , can form arrays

Address correspondence to Zhi-Wei Shan, zwshan@mail.xjtu.edu.cn; Ju Li, liju@mit.edu; Evan Ma, ema@jhu.edu

and patterns of microscale MG structures [11, 12]. This suggests that submicron-sized MGs may be excellent building blocks for small-scale architectures. However, in order to achieve intricate architectures, shape change and the joining of individual components are necessary. For bulk glass, effective methods, such as blowing and molding in the liquid (or supercooled liquid) state [12, 13] and welding processes, have been developed in recent years [14, 15]. However, for microscale MG components, the shaping and joining of individual components become a rather challenging issue. Challenges pertaining to processing in the microscopic range arise from a number of unprecedented needs. First, the location and manipulation of a specific MG component requires sub-micron precision. Second, the heating has to be both fast and extremely focused, such that the component reaches a high enough local temperature to allow mass flow while not affecting other components and devices, only nanometers or micrometers away. The creation of this very small heat-affected zone requires intense but highly localized energy input. Third, rapid cooling of the heated (molten) sample is necessary to ensure that the solidified product after reshaping/joining is an MG with a completely amorphous structure, the same as the original and as other components in the system, without crystallization [4]. In the article, we demonstrate a new nano-scale processing method that produces a sharp temperature spike locally in the particular component of interest, achieving all the above goals simultaneously. This novel method was inspired by the spontaneous reshaping of micron-sized MG beams, which we observed serendipitously and later traced to the ground potential fluctuation $V(t)$, which was not there by design.

2 Experimental

The experimental design is displayed in Fig. 1(a). A W tip and a conductive sample are connected to ground points G_1 and G_2 , respectively, exhibiting a $V(t)$ as seen in Fig. 1(b), measured by a voltmeter. Similar $V(t)$ are observed in many other nano-manipulation and *in situ* observation systems; for the purpose of reproducing the phenomena described next, this random energy reservoir can be replaced by an alternative, more

controlled electrical power source. The presence of a regular 50-Hz component (Fig. 1(b)) means the external power supply contributes at least partly to the fluctuation of $V(t)$. On top of this regular component, we also see a randomly fluctuating component with amplitude up to ± 0.3 V. Such a fluctuating electrical energy supply can generate significant effects on small asperities prior to contact with the W tip. This is because electromechanical systems have effective capacitances C ($C \equiv Q/V$) as well as inductances L ($V \equiv L \cdot dI/dt$) distributed throughout, where C and L are geometry-dependent. Effective circuit C and L may have dramatic impacts on small asperities prior to contact because of electrical discharge, since $I = dQ/dt = C \cdot dV/dt$. A relatively large current I may need to pass through a very small asperity in a very short time to heat it to a very high temperature. In Fig. 1(a), R is an adjustable macro-scale resistor

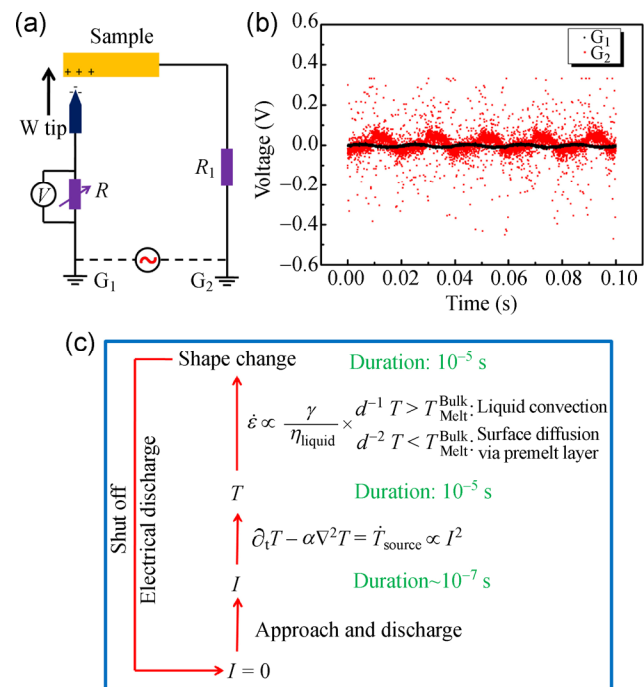


Figure 1 The schematic of NED and its working principle. (a) Schematic for the experimental set up. The W tip and microscale sample are grounded at G_1 and G_2 , respectively. The instantaneous electrical pulse is monitored by an oscilloscope (voltmeter) in parallel with a tunable electrical resistor, R . The black arrow indicates the moving direction of the W tip. (b) The measured ground potential evolution $V(t)$ of G_1 and G_2 in our lab. (c) A flow chart showing the time scale of the NED-induced pulsed current, temperature evolution, and mass transport for shape change in micron-sized beams.

introduced externally to impart control, and R_1 is the systematic electrical resistance. The W tip is driven by a Kleindiek Nanotechnik control system, connected with G_1 , allowing movements in all three directions plus a rotational degree of freedom. The smallest step-size of the control system is 5 nm. When the dimensions of the W tip and the sample are on conventional size scales, e.g., millimeters and centimeters, the electrical field E resulting from the minute potential difference is too small to generate any electrical discharge when the tip and sample are driven toward each other. However, the situation changes dramatically in the micro- and nano-scale. The W tip and sample in our design are now extremely “sharp” tips with radii of curvature in the submicron range. It is well known that a sharp tip dramatically decreases the threshold voltage for field electron emission and discharge, such as in carbon nanotubes [16, 17]. When the W tip is brought towards the sample, $V(t)$ will induce electrical charges with opposite signs on both sides. As the W tip is brought within distances of tens of nm or less, depending on the $V(t)$ of the sample connected to G_2 , the tip-enhanced electrical field E increases dramatically to reach the critical value for nanoscale electrical discharge (NED), due to the large local field enhancement factor caused by sharp geometry [18–22], even at very low voltages. Figure 1(c) is a flowchart

showing the time scales of the NED-induced pulse current, temperature evolution, and shape change of the sample.

3 Results and discussion

We first show that NED can cause micron-sized Mo single-crystal beams to undergo ultrafast and dramatic shape changes. In order to minimize interference in the procedure as well as to monitor the entire process, both the fabrication of samples and the tests were conducted inside a Helios Nanolab dual-beam focused ion beam (FIB). The electrical signals were monitored simultaneously using a Tektronix oscilloscope. Mo is a refractory metal with a bulk melting temperature $T_M = 2,896$ K. Figure 2 shows the typical shape change of a Mo single-crystal beam (see Electronic Supplementary Material (ESM) and Fig. S1 for the detailed sample preparation procedure). When the W tip was driven to approach the Mo beam, as shown in Fig. 2(a), NED occurred suddenly and caused the beam to split and form two parts with spherical ends, as shown in Fig. 2(b). The estimated total volume after this dramatic shape change was very close to that of the initial beam, suggesting minimal mass loss due to evaporation. Notably, the W tip and the surrounding structure did not show detectable changes during this process, as

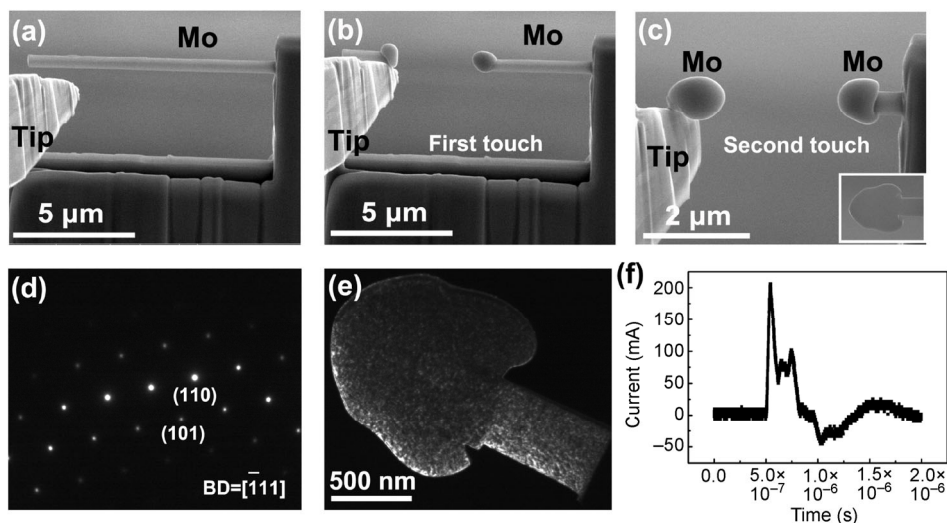


Figure 2 NED-induced ultrafast and dramatic shape change in a single-crystal Mo beam. (a) The W tip on the left was driven to approach the Mo beam with a size of 520 nm × 480 nm × 10 μm. (b) The morphology of the Mo beam after the first NED process. (c) The beam continued to shrink and formed a “mushroom” structure during the second NED. The inset shows a thinned mushroom structure. (d) and (e) are the selected-area diffraction pattern and cross-sectional view of the “mushroom” head, respectively. Both confirm that the cap of the Mo “mushroom” is the same single crystal as its root. (f) Current evolution measured during the second NED.

seen in Fig. 2(b). The corresponding transient NED current (Fig. 2(f)) was recorded by an oscilloscope in parallel with a resistor ($R = 1 \Omega$, as in Fig. 1(a)). The electrical current lasted $\sim 1 \mu\text{s}$. A second approach generated another NED, which transformed the beam—still rooted to its parent body—into a “mushroom” geometry (Fig. 2(c)) in a very short time, as shown in Movie S1 in ESM. To reveal its internal structure, the “mushroom” structure was thinned to a 100-nm-thick slice and examined by a JEOL 2100F Transmission Electron Microscope (TEM). The selected-area diffraction pattern (Fig. 2(d)), and dark-field TEM observations (Fig. 2(e)) demonstrate that the “mushroom” interior remained monocrystalline with a lattice orientation matching that of its parent body. In traditional welding or laser-melting processes, the melt zone becomes polycrystalline. Rapid re-growth of the same crystalline orientation may have occurred back into the liquid as it was being quenched, since the liquid was still connected to the single-crystal parent. The defects observed in Fig. 2(e) are attributed to Ga^{3+} -ion irradiation and implantation.

The observed phenomenon can be rationalized as follows: based on the thermal and physical parameters of Mo [23], the transient input energy ($\sim 26 \text{ nJ}$) from Joule heating by the recorded electrical pulse in Fig. 2(f), would transform part of the Mo beam to the molten state; surface-tension-driven mass transport will lead to the ultrafast shape change of the Mo beam, which will in turn break down the electrical connection, thus shutting off the NED energy feed, as seen in the flowchart of Fig. 1(c). Afterward, the heat in the Mo beam dissipated through thermal conduction to the connected base material. The thermal diffusivity (α) of Mo is about $5.4 \times 10^{-5} \text{ m}^2\text{s}^{-1}$ at room temperature. The characteristic time for temperature decay (τ_T) obeys the rule $\tau_T \sim L^2/\alpha$, where L is the thermal diffusion length in beams ($\sim 10 \mu\text{m}$). With these figures, the time for Mo to cool from T_M to room temperature is estimated to be 10^{-5} s , consistent with the results predicted by finite element modeling (Fig. S2 in ESM), providing a cooling rate $\sim 10^8 \text{ K}\cdot\text{s}^{-1}$. This means that the mass transport permitting shape change was terminated during this short period, with an extremely fast strain rate $\sim 10^6 \text{ s}^{-1}$. The different morphologies (sphere-like versus mushroom) after two consecutive

NEDs is attributed to the shortening of the thermal diffusion distance, causing faster cooling in the second case, causing freeze-in of an unstable morphology. Very recently, a similar rapid heating-and-quenching route using electrical pulses has been successfully used for experimentally fabricating monatomic MG at even smaller scales (tens of nm) with cooling rates as high as $10^{13} \text{ K}\cdot\text{s}^{-1}$ [24]. The application described in this study works at a relatively lower cooling rate, permitting the preservation of the original material's atomic structure during welding. NED, taking advantage of the ground potential, can induce the ultrafast electrical pulse. This means that localized ultra-fast heating can be achieved in a wide range of sample shapes, as opposed to being limited to sample regions where electrical resistance (heating) is solely determined by the initial geometry. The cooling rate in the $\sim 40\text{-nm}$ long Ta crystal is larger than $10^{13} \text{ K}\cdot\text{s}^{-1}$, exceeding the critical cooling rate for the vitrification of Ta atoms. In comparison, the cooling rate in this study for the Mo component at the microscale is significantly higher than that at macro scale but still much lower than the critical rate for Mo vitrification.

Similar fast mass transfer was also observed in $\text{Cu}_{49}\text{Zr}_{51}$ MG beams, as shown in Fig. 3. $\text{Cu}_{49}\text{Zr}_{51}$ MG has a T_g of $\sim 700 \text{ K}$ and a liquidus temperature T_l of $\sim 1,200 \text{ K}$ [25]. NED occurred when the W tip approached the sample, and the original beam shrank into a sphere without breaking, as seen in Fig. 3(b) and Movie S2 in ESM. The observed spherical shape indicates that the operation is driven by surface tension. It is interesting that the structure remained predominantly amorphous, as shown in Fig. 3(c), except for a few isolated nanocrystals (of the scale of 10 nm) on the surface. Apparently, due to the large heat sink that the sample is attached to, the quench rate of the small molten beam ($> 10^7 \text{ K}\cdot\text{s}^{-1}$, in ESM) is high enough to quench the liquid back into a glass. Such rapid cooling has also been reported during the fabrication of submicron-sized carbon glass beads using an electrical arc method [26]. Notably, the shape change and mass transport also depend on the sample size. Fig. 3(d) shows a Cu–Zr glass beam with a larger diameter d . The shrinkage of the beam was suppressed in the middle, in contrast to the smaller beam that shrank into a sphere in Fig. 3(b). This is because Joule

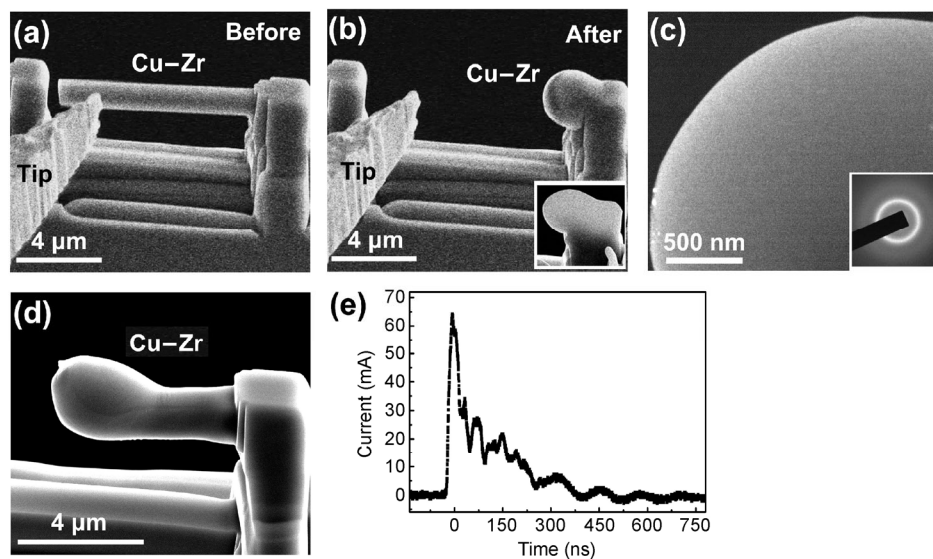


Figure 3 NED-induced ultrafast and dramatic shape change in $\text{Cu}_{49}\text{Zr}_{51}$ MG beams. (a) The original morphology of the Cu–Zr beam ($1,200 \text{ nm} \times 700 \text{ nm} \times 9 \text{ }\mu\text{m}$). (b) After NED, the Cu–Zr beam shrunk very fast to the right base, forming a hemisphere-like structure. The inset, framed by the red box, is the thinned sample for cross-sectional view examination. (c) The centered dark-field TEM image and the corresponding selected-area diffraction pattern of the cross-sectional view confirmed that the hemisphere-like structure is still amorphous. (d) A larger-size Cu–Zr beam ($1.5 \text{ }\mu\text{m} \times 1.5 \text{ }\mu\text{m} \times 8 \text{ }\mu\text{m}$) exhibited less mass transport. (e) Current evolution measured during the NED process.

heating-induced ΔT decreases dramatically with increasing sample size (see ESM).

Comparing the morphologies in Fig. 2 and Fig. 3, the shrinkage of the Mo beam was terminated in the middle to produce a mushroom shape, while the Cu–Zr sphere reached the base material. Thermodynamically, both the molten Mo and Cu–Zr beams would be driven towards a low-energy spherical shape by surface tension, but the mass transport would be kinetically affected by surface tension, thermal diffusivity, and the dimensions of the studied samples. The thermal diffusivity of Cu–Zr glass is one order of magnitude smaller than that of refractory Mo [27, 28] and the Cu–Zr MG beam is as long as the Mo beam, thus it remained at a high temperature for longer than the Mo beam (shown in finite element analysis in Fig. S2). The extended time spent at a high temperature would contribute to greater mass transport, causing the formation of a sphere. Besides the aforementioned factors, the morphological outcome of the mass transport also depends on the tunable resistor R_T , which may influence the discharge pulse intensity (see details in ESM).

As the shape change behaviors are seen to be generic, some analysis is in order. The observed phenomena involve electrical (τ_E), thermal (τ_T), and mass (τ_M) transport, coupled with intrinsic characteristic timescales denoted in the brackets. A logic flowchart is shown in Fig. 1(c). From Fig. 2(e) and 3(e), we know that the NED persisted for $\tau_E \sim 10^{-6}$ s. Electrical discharge is a complex phenomenon [18–22]. Once NED starts, some atoms may evaporate from the solid sample's surface and be ionized into plasma, which sustains the discharge, forming a nano- or micro-arc [21, 22] even though the two electrodes are not in physical contact. Eventually, as the tips recede far enough, the NED would stop. Let the beam have a characteristic length L and diameter d , and the receding “mushroom” tip has a characteristic radius of curvature r . Initially, $r \propto d$. As the beam is connected to a large heat sink, $\tau_T = L^2/\alpha$. For crystalline Mo, α approaches $5 \times 10^{-5} \text{ m}^2\text{s}^{-1}$, so for $L = 5 \text{ }\mu\text{m}$, τ_T is approximately 5×10^{-7} s. We thus see that τ_E and τ_T are roughly of equal scale. Next, we show that the intrinsic mass transport timescale τ_M could be much faster than τ_E and τ_T as well, if convective flow occurs. If the “mushroom” region (e.g.,

Fig. 2(c)) with characteristic curvature r has fully melted, $T > T_M$ and the liquid has shear viscosity η_{liquid} , the liquid tip would recede under the Young-Laplace pressure difference $\Delta P \sim \gamma/r$, with strain rate $\sim \Delta P/\eta_{\text{liquid}}$ and maximum receding velocity $v_{\text{max}} \sim r\Delta P/\eta_{\text{liquid}} \sim \gamma/\eta_{\text{liquid}}$. Taking $\gamma = 2.08 \text{ J}\cdot\text{m}^{-2}$ and $\eta_{\text{liquid}} = 5.6 \times 10^{-3} \text{ Pa}\cdot\text{s}$ for liquid Mo at its melting point [23], we predict $v_{\text{max}} \sim 400 \text{ m}\cdot\text{s}^{-1}$, which is independent of the length scale. This is verified by a direct molecular dynamics (MD) simulation of a fully molten Mo mushroom, which receded by 20 nm in 84 ps, with $v_{\text{max}} \sim 250 \text{ m}\cdot\text{s}^{-1}$, as shown in Fig. 4. Thus, if the mushroom is fully molten, the shape change timescale would be $\tau_M \sim r/v_{\text{max}}$. This suggests that even for a large mushroom, $r = 1 \mu\text{m}$, τ_M would still be 2–3 orders of magnitude smaller than

τ_E and τ_T . This means that if convection is activated, the intrinsic shape change ability is so high that τ_M would not be the process-limiting timescale. In this mass-transport scenario (scenario I), the shape change would be thermally limited, i.e., the liquid portion would “instantaneously” take its minimum-capillary-energy configuration (with respect to the solid) seen at the timescale of τ_E and τ_T , which clearly control the phase change.

In an alternative mass-transport scenario (scenario II), we assume there is pre-melting of the surface [29, 30], but no bulk melting, as the local temperature is not high enough ($T < T_M$). In this case, Coble creep [30] of the mushroom would occur, i.e., a surface-diffusion-driven shape change without convection.

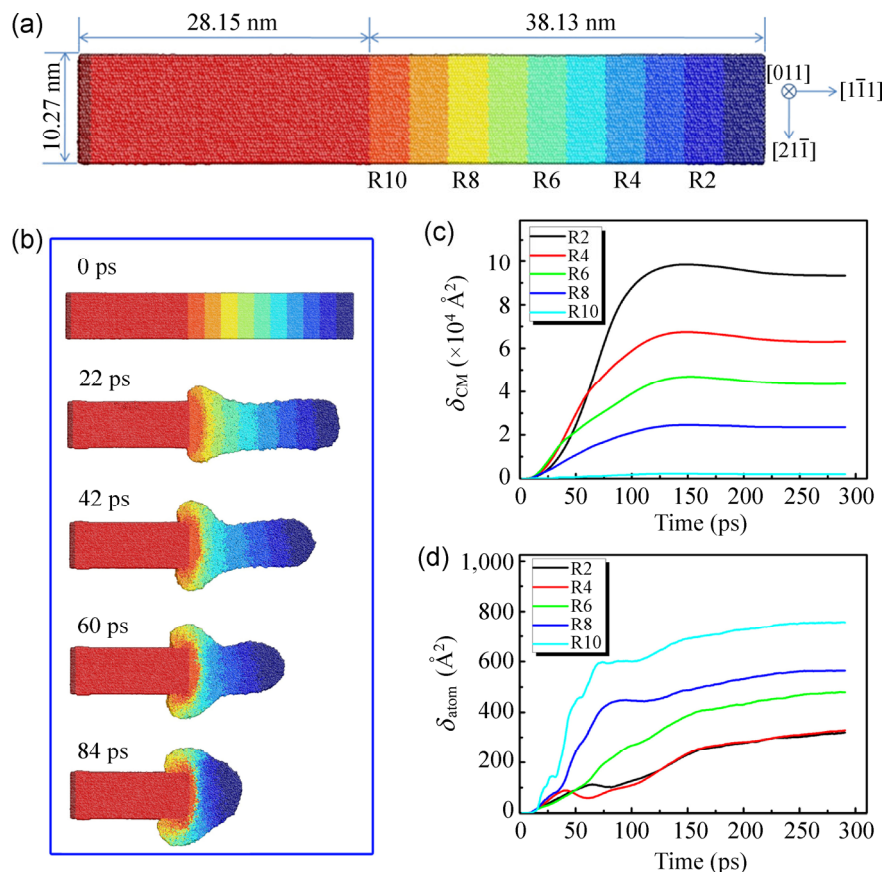


Figure 4 MD simulation of the mass transportation mechanism during the shrinking process of a partially melted Mo nanobeam. (a) The nanobeam with its axial direction $[1\bar{1}1]$ is divided into three regions: left dark red region (fixed), middle bright red region (kept at 441 K) and right observation region (instantaneously heated to 4,800 K). The last region is divided into ten small regions, marked as R_i , $i = 1-10$, from the right free end to the left. (b) Morphology evolution of Mo nanobeam under surface tension. A mushroom shape is formed in 84 ps. Note that here we ignore thermal conduction to the external surroundings. (c) The mean square displacements of the centers of mass (δ_{CM}) of the different marked regions versus time. (d) The mean square displacement of individual atoms (δ_{atom}) versus time. The fact that $\delta_{\text{CM}} \gg \delta_{\text{atom}}$ indicates that convection dominates shrinkage, rather than the self-diffusion of atoms.

However, a semi-quantitative calculation (see ESM) indicated that the shape change capability through Coble creep would be 6–9 orders of magnitude less than that in scenario I. By this reckoning, the characteristic shape change timescale τ_M would fall in the range of seconds. Indeed, we have recently observed Coble creep-induced shape change in Sn at $T = 0.6 T_M$ with *in situ* TEM, at timescales of 0.1 s [30]. Scenario II, therefore, cannot explain the experimental results here, because (a) with $\tau_T \ll \tau_M$ surface diffusion would long have been “frozen out” as the temperature recovers to room temperature in Mo, and (b) with the recording time resolution of the *in situ* SEM movies, we should have recorded the shape change process if τ_M fell into the range of 0.1 s, as is the case with Sn, but we did not. For these reasons, scenario II is self-contradictory and is excluded. We are left with scenario I, thermally limited capillary-driven convective flow, as the only possible scenario. The heating, quenching, and shape change are thus all predicted to occur within the characteristic timescale of 10^{-6} s.

We next demonstrate that NED can be used for ultrafast mass transport and joining of small-volume materials, distinct from the micro- and nanoscale joining methods reported so far [31, 32]. A piece of Mo single crystal adhered to the W tip was approached

the Mo base material (Fig. 5(a)). With NED occurring between the two ends, the induced mass transport at the interface joins of the two parts (Fig. 5(b)). After the joining, we retracted the W tip to exert a mechanical load on the entire structure. The beam eventually fractured at the right-hand-side end (Fig. 5(c)), rather than at the welded regions of the W/Mo and Mo/Mo joints, indicating that the welded regions were mechanically as strong as other parts of the beam. The welded region also produced no obvious Kapitza (interfacial) electrical resistance. Thus, the weld is both mechanically and electrically sound.

A second example is shown in Fig. 5(d)–(f), where 3 separate Cu–Zr glass beams were fabricated using FIB. Upon applying NED between the W tip and Beam 1, mass transport was induced in Beam 1 (as a sacrificial beam) to fill the gap between Beam 2 and Beam 3 (Movie S3 in ESM). FIB-cutting revealed that the unification was perfect in the joint, as seen in the cross-sectional view in Fig. 5(f).

4 Conclusions

The above examples highlight the advantages of NED-induced welding. It is highly localized, the heat-affected zone is very small, and the structure in the joint

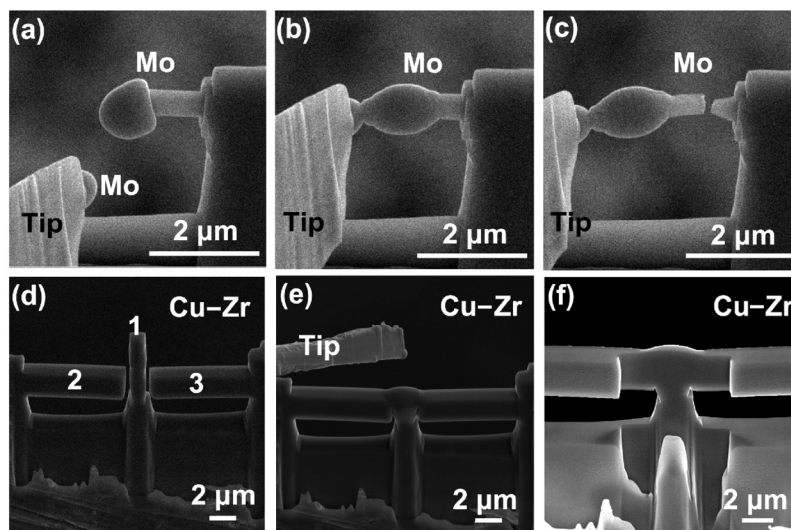


Figure 5 Application of NED for ultrafast mass transportation and welding of small-volume materials. (a) A piece of refractory single-crystal Mo adhered to a W tip is driven to approach the Mo base material. (b) After the NED process, the two parts were welded together. (c) The beam fractured at the right end when the W tip was retracted, which indicates the welding region is mechanically strong. (d) Three separate Cu–Zr glass beams are fabricated for three-end welding. (e) NED between the W tip and Beam 1 resulted in the welding of the three beams. (f) A cross-sectional view of the welding zone.

closely resembles the internal structure of the rest of the components, whether crystalline or amorphous. It is also chemically clean, without the need for a solder, flux, or braze layer. Through careful *in situ* electrical measurement, electron microscopy, and modeling, we have determined that these morphological changes occur by the thermally limited capillary-driven convective flow of liquid melt, rather than by surface-diffusion-driven Coble creep [30], which would be substantially slower. The electrical discharge, heating, quenching, and shape change should all occur within a timescale of 10^{-6} s. The fact that one can use NED to make high-quality welds between high-melting-point metals ($T_M(\text{Mo}) = 2,896$ K, $T_M(\text{W}) = 3,695$ K) without affecting nearby nanostructure is technologically significant. Investigation on the use of NED to weld metal to semiconductors, as well as welding between semiconductors, is currently under way, and will be reported in a future study.

Acknowledgements

This work was supported by the grants from NSFC (Nos. 50925104, 51231005 and 51321003) and 973 (Program of China) (Nos. 2010CB631003, 2012CB619402). We also appreciate the support from the 111 Project of China (No. B06025). Both E. M. and J. L. carried out this work under an adjunct professorship at XJTU. J. L. acknowledges support by NSF (No. DMR-1120901). E. M. was supported at JHU by US-NSF (No. DMR-0904188).

Electronic Supplementary Material: Supplementary material is available in the online version of this article at <http://dx.doi.org/10.1007/s12274-014-0685-7>.

References

- [1] Uchic, M. D.; Dimiduk, D. M.; Florando, J. N.; Nix, W. D. Sample dimensions influence strength and crystal plasticity. *Science* **2004**, *305*, 986–989.
- [2] Shan, Z. W.; Mishra, R. K.; Asif, S. A. S.; Warren, O. L.; Minor, A. M. Mechanical annealing and source-limited deformation in submicrometre-diameter Ni crystals. *Nat. Mater.* **2008**, *7*, 115–119.
- [3] Yu, Q.; Shan, Z. W.; Li, J.; Huang, X.; Xiao, L.; Sun, J.; Ma, E. Strong crystal size effect on deformation twinning. *Nature* **2010**, *463*, 335–338.
- [4] Wang, C. C.; Mao, Y. W.; Shan, Z. W.; Dao, M.; Li, J.; Sun, J.; Ma, E.; Suresh, S. Real-time, high-resolution study of nanocrystallization and fatigue cracking in a cyclically strained metallic glass. *Proc. Nat. Acad. Sci. U.S.A.* **2013**, *110*, 19725–19730.
- [5] Tian, L.; Cheng, Y. Q.; Shan, Z. W.; Li, J.; Wang, C. C.; Han, X. D.; Sun, J.; Ma, E. Approaching the ideal elastic limit of metallic glasses. *Nat. Comm.* **2012**, *3*, 609.
- [6] Wang, C. C.; Ding, J.; Cheng, Y. Q.; Wan, J. C.; Tian, L.; Sun, J.; Shan, Z. W.; Li, J.; Ma, E. Sample size matters for al88fe7gd5 metallic glass: Smaller is stronger. *Acta Mater.* **2012**, *60*, 5370–5379.
- [7] Guo, H.; Yan, P. F.; Wang, Y. B.; Tan, J.; Zhang, Z. F.; Sui, M. L.; Ma, E. Tensile ductility and necking of metallic glass. *Nat. Mater.* **2007**, *6*, 735–739.
- [8] Jang, D. C.; Greer, J. R. Transition from a strong yet brittle to a stronger and ductile state by size reduction of metallic glasses. *Nat. Mater.* **2010**, *9*, 215–219.
- [9] Jiang, Q. K.; Liu, P.; Cao, Q. P.; Wang, C.; Li, X. L.; Gao, X. Y.; Wang, X. D.; Zhang, D. X.; Han, X. D.; Zhang, Z.; Jiang, J. Z. The effect of size on the elastic strain limit in Ni60Nb40 glassy films. *Acta Mater.* **2013**, *61*, 4689–4695.
- [10] Deng, Q. S.; Cheng, Y. Q.; Yue, Y. H.; Zhang, L.; Zhang, Z.; Han, X. D.; Ma, E. Uniform tensile elongation in framed submicron metallic glass specimen in the limit of suppressed shear banding. *Acta Mater.* **2011**, *59*, 6511–6518.
- [11] Kumar, G.; Tang, H. X.; Schroers, J. Nanomoulding with amorphous metals. *Nature* **2009**, *457*, 868–U128.
- [12] Schroers, J. Processing of bulk metallic glass. *Adv. Mater.* **2010**, *22*, 1566–1597.
- [13] Johnson, W. L.; Kaltenboeck, G.; Demetriou, M. D.; Schramm, J. P.; Liu, X.; Samwer, K.; Kim, C. P.; Hofmann, D. C. Beating crystallization in glass-forming metals by millisecond heating and processing. *Science* **2011**, *332*, 828–833.
- [14] Swiston, A. J.; Hufnagel, T. C.; Weihs, T. P. Joining bulk metallic glass using reactive multilayer foils. *Scr. Mater.* **2003**, *48*, 1575–1580.
- [15] Kawamura, Y.; Ohno, Y. Spark welding of Zr55Al10Ni5Cu30 bulk metallic glasses. *Scr. Mater.* **2001**, *45*, 127–132.
- [16] De Heer, W. A.; Chatelain, A.; Ugarte, D. A carbon nanotube field-emission electron source. *Science* **1995**, *270*, 1179–1180.
- [17] Wang, Q. H.; Corrigan, T. D.; Dai, J. Y.; Chang, R. P. H.; Krauss, A. R. Field emission from nanotube bundle emitters at low fields. *Appl. Phys. Lett.* **1997**, *70*, 3308–3310.
- [18] Chatterton, P. A. A theoretical study of field emission initiated vacuum breakdown. *Proc. Phys. Soc. London* **1966**, *88*, 231–245.

- [19] Charbonnier, F. M.; Bennette, C. J.; Swanson, L. W. Electrical breakdown between metal electrodes in high vacuum. I. Theory. *J. Appl. Phys.* **1967**, *38*, 627–640.
- [20] Utsumi, T. Cathode- and anode-induced electrical breakdown in vacuum. *J. Appl. Phys.* **1967**, *38*, 2989.
- [21] Smith, W. A.; Elliot, C. T.; Pulfrey, D. L. A photographic study of electrical breakdown at small gaps in vacuum. *J. Phys. D-Appl. Phys.* **1969**, *2*, 1005.
- [22] Davies, D. K.; Biondi, M. A. Detection of electrode vapor between plane parallel copper electrodes prior to current amplification and breakdown in vacuum. *J. Appl. Phys.* **1970**, *41*, 88.
- [23] Iida, T.; Guthrie, R. Predictions for the sound velocity in various liquid metals at their melting point temperatures. *Metal. and Materi. Trans. B* **2009**, *40*, 959–966.
- [24] Zhong, L.; Wang, J.; Sheng, H.; Zhang, Z.; Mao, S. X. Formation of monatomic metallic glasses through ultrafast liquid quenching. *Nature* **2014**, *512*, 177–180.
- [25] Jiang, Q. K.; Wang, X. D.; Nie, X. P.; Zhang, G. Q.; Ma, H.; Fecht, H. J.; Bednarcik, J.; Franz, H.; Liu, Y. G.; Cao, Q. P.; Jiang, J. Z. Zr-(Cu,Ag)-Al bulk metallic glasses. *Acta Mater.* **2008**, *56*, 1785–1796.
- [26] de Heer, W. A.; Poncharal, P.; Berger, C.; Gezo, J.; Song, Z. M.; Bettini, J.; Ugarte, D. Liquid carbon, carbon-glass beads, and the crystallization of carbon nanotubes. *Science* **2005**, *307*, 907–910.
- [27] Choy, C. L.; Tong, K. W.; Wong, H. K.; Leung, W. P. Thermal conductivity of amorphous alloys above room temperature. *J. Appl. Phys.* **1991**, *70*, 4919–4925.
- [28] Lide, D. R. *CRC handbook of chemistry and physics*; CRC Press, 2009.
- [29] Mishin, Y.; Asta, M.; Li, J. Atomistic modeling of interfaces and their impact on microstructure and properties. *Acta Mater.* **2010**, *58*, 1117–1151.
- [30] Tian, L.; Li, J.; Sun, J.; Ma, E.; Shan, Z.-W. Visualizing size-dependent deformation mechanism transition in Sn. *Scientific Reports* **2013**, *3*, 2113.
- [31] Jin, C. H.; Suenaga, K.; Iijima, S. Plumbing carbon nanotubes. *Nat. Nanotechnol.* **2008**, *3*, 17–21.
- [32] Lu, Y.; Huang, J. Y.; Wang, C.; Sun, S. H.; Lou, J. Cold welding of ultrathin gold nanowires. *Nat. Nanotechnol.* **2010**, *5*, 218–224.

Electronic Supplementary Material

Ultrafast shape change and joining of small-volume materials using nanoscale electrical discharge

Cheng-Cai Wang^{1,5}, Qing-Jie Li^{1,4}, Liang Chen^{1,2}, Yong-Hong Cheng², Jun Sun¹, Zhi-Wei Shan¹ (✉), Ju Li^{1,3} (✉), and Evan Ma^{1,4} (✉)

¹ Center for Advancing Materials Performance from the Nanoscale (CAMP-Nano) & Hysitron Applied Research Center in China (HARCC), State Key Laboratory for Mechanical Behavior of Materials, Xi'an Jiaotong University, Xi'an 710049, China

² State Key Laboratory of Electrical Insulation and Power Equipment, Xi'an Jiaotong University, Xi'an 710049, China

³ Department of Nuclear Science and Engineering and Department of Materials Science and Engineering, Massachusetts Institute of Technology, 77 Massachusetts Avenue, Cambridge, Massachusetts 02139, USA

⁴ Department of Materials Science and Engineering, Johns Hopkins University, Baltimore, Maryland 21218, USA

⁵ SJS Limited, 101 Xihuan Road, Jingzhou, Hubei 434024, China

Supporting information to DOI 10.1007/s12274-015-0685-7

Table of Contents

- S1 Materials and sample preparation
 - S2 Temperature rise (ΔT) calculations
 - S3 Finite element analysis of thermal conduction
 - S4 MD simulation of mass transport of Mo single crystal beam
 - S5 Influence of external electrical resistor on the NED
 - S6 Description of supporting movies and their link addresses
- References

S1 Materials and sample preparation

A piece of Mo single crystal (3 mm × 3 mm × 0.5 mm) was cut from a large rod with diameter 30 mm. Cu₄₉Zr₅₁ metallic glass ribbons with thickness less than 200 μm were made by a melt-spun technique. The schematic sample preparation procedure was shown in Fig. S1. A square sample with 3-mm in side-length was mechanically and chemically polished on both sides to a thickness less than 20 μm (Fig. S1(b)). The chemical polishing condition for Mo is an ethanol solution containing 5% perchloric acid. The sample is then adhered on special

Address correspondence to Zhi-Wei Shan, zwshan@mail.xjtu.edu.cn; Ju Li, liju@mit.edu; Evan Ma, ema@jhu.edu

designed copper sample mount using a silver glue which is electrically conductive (Fig. S1(c)). After this, the sample mount was transferred to the chamber of a dual-beam focused ion beam (FIB, Helios NanoLab 600i). The sample edge was first coarsely thinned under 30 kV Ga ion beam with current 9.3 nA to less than 5 μm (Fig. S1(d)); secondly, the milling current was decreased down to 97 pA to refine sample into designed geometry (Fig. S1(e)); Finally, in order to minimize the ion beam damage, lower voltage 16 kV with current 45 pA was used to polish the sample.

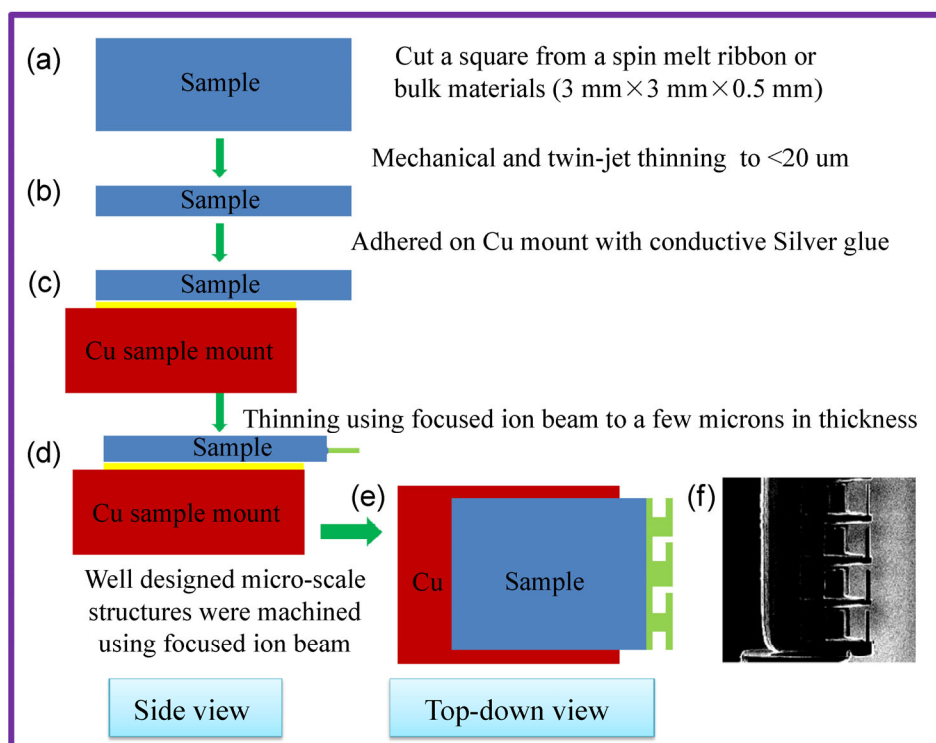


Figure S1 Schematic of the sample preparation procedures. (a)–(d) are side views showing the thinning procedure, including mechanical thinning, electrical twin-jet polishing and micromachining using focused ion beam. (e) Top-down view of the fabrication of microscale cantilever beams. (f) SEM image of the fabricated microscale beams.

S2 Temperature rise (ΔT) calculations

The instantaneous electrical pulse-induced resistive heating (see in Fig. 2(f)) could contribute into temperature rise (ΔT) and fusion of heat, as the following relation:

$$I^2 R t = C_p m \Delta T + \Delta H \quad (1)$$

Where I is the pulse current, t is the duration time of pulse and R is the electrical resistance of sample; on the right hand side of the equation, C_p is the specific heat capacity, m is the mass, ΔH is the fusion of heat. Consider the geometry of the beam (d is the diameter and L is the length of the beam), the electrical resistance R is $\rho_e L / d^2$, where ρ_e is the electrical resistivity; m equals to $\rho_d d^2 L$, where ρ_d is the density, therefore

$$C_p \Delta T + \Delta H_m = I^2 t (\rho_e / \rho_d) d^{-4} \quad (2)$$

Where ΔH_m is the specific heat of fusion ($\Delta H/m$). For simplicity, we do not consider the modest change of physical parameters with the temperature, such as the electrical resistivity and specific heat of capacity. All these calculations are based on the input information from Figs. 2 and 3. For Mo beam, substituting the physical parameters [S1], the calculated input Joule heating energy is only 25.6 nJ but causes a temperature rise (ΔT) about 2,700 K (seen in Table 1), even reaches its melting point (2,890 K). On the other hand, for the binary Cu–Zr metallic glass alloy, C_p of Cu–Zr-based metallic glass increases from 25 to 45 J/mol·K when ΔT goes up to thousands of Kelvin from room temperature [S2], showing consistent trend reported in other alloys [S3]. And because most metalloid-free bulk metallic glasses exhibit a conservation of the original volumes of “mechanically-mixed” constituent elemental metals [S4], the calculated molar volume of $\text{Cu}_{49}\text{Zr}_{51}$ metallic glass is 10.67 cm³/mol, then C_p should be in the range of 320–580 J/kg·K in the temperature range [S2]. ρ_e of Cu–Zr-based metallic glasses and corresponding liquids is relatively large (~100–300 $\mu\Omega\cdot\text{cm}$) [S5–S8], and frequently exhibits a negative temperature coefficient [$1/(1/\rho_e)d\rho_e/dT \leq 1 \times 10^{-4} \text{ K}^{-1}$] [S6, S7]. When an electrical pulse (0.2 A with duration 200 nanosecond as seen in Fig. 3(e)) passes through the beam, take $\Delta H_m \sim 8 \text{ KJ/mol}$ and $\rho_e \sim 200 \mu\Omega\cdot\text{cm}$ in Cu–Zr MG [S2, S8], the calculated ΔT is $\sim 3,600 \text{ K}$ without considering thermal conduction, indicating the Cu–Zr beam becomes complete liquid ($T_1 \sim 1,200 \text{ K}$) [S2].

Table S1 Thermal calculations of Mo and Cu–Zr beam. All input information is from Figs. 2 and 3, detailed information of the physical parameters seen in the main text

Sample	Geometry	Input	ρ_e ($\mu\Omega\cdot\text{cm}$)	ρ_d (g/cm^3)	C_p ($\text{J}/(\text{kg}\cdot\text{K})$)	ΔH_m (J/Kg)	Q (nJ)	ΔT (K)
Mo	$d = 0.5 \mu\text{m}$ $L = 10 \mu\text{m}$	$I = 0.2 \text{ A}$ $t = 300 \text{ ns}$	5.34	10.2	250	3.33×10^5	25.6	2,700
Cu–Zr	$d = 1 \mu\text{m}$ $L = 10 \mu\text{m}$	$I = 0.2 \text{ A}$ $t = 200 \text{ ns}$	200	7.3	320–580	1.03×10^5	160	3,600

S3 Finite element analysis of thermal conduction

Finite element method was used to calculate the transient thermal conduction in $\text{Cu}_{49}\text{Zr}_{51}$ metallic glass and Mo single crystal beam. The same model composing a cubic ($10 \mu\text{m} \times 10 \mu\text{m} \times 10 \mu\text{m}$) and a cantilever ($1 \mu\text{m} \times 1 \mu\text{m} \times 10 \mu\text{m}$) was built up for these two materials. Following material parameters were used: density of $\text{Cu}_{49}\text{Zr}_{51}$ ($7.3 \text{ g}/\text{cm}^3$) and Mo ($10.2 \text{ g}/\text{cm}^3$), specific heat capacity of $\text{Cu}_{49}\text{Zr}_{51}$ ($0.32 \text{ J}/\text{g}\cdot\text{K}$) and Mo ($0.251 \text{ J}/\text{g}\cdot\text{K}$), thermal conductivity of Cu–Zr MG ($1.026 + 0.0165T$, $\text{W}/\text{m}\cdot\text{K}$ and T is temperature, K) and Mo ($138 \text{ W}/\text{m}\cdot\text{K}$) [S2, S8]. For simplicity, the weak dependence of these physical parameters on temperature was not considered except the thermal conductivity of Cu–Zr-based metallic glass. The initial temperatures of beam are 3,000 K for Cu–Zr MG and 4,912 K (boiling temperature) for Mo SC while the temperature of base cubic is 300 K. The transient temperature evolutions of the beam were shown in Fig. S2. Both of these two materials were quenched to room temperature within very short time ($\sim 10^{-5} \text{ s}$), corresponding cooling rate reaches $10^8 \text{ K}/\text{s}$. And cooling of Cu–Zr beams was slower due to its smaller thermal conductivity than that of Mo beam, which indicates Cu–Zr beams could stay longer at high temperature even with a lower starting T as seen in Fig. S2(e).

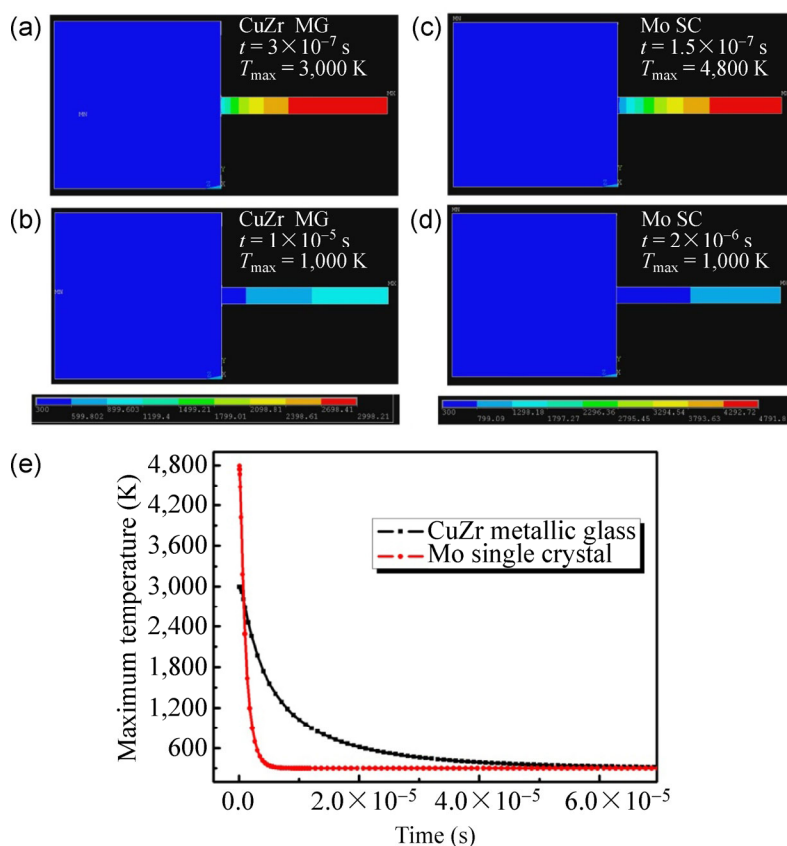


Figure S2 Finite element analysis of the transient temperature evolution in Cu–Zr metallic glass and Mo single crystal beam (same geometry) due to thermal conduction. (a) and (b) show the temperature distribution in Cu–Zr MG beam when the time respectively equals to 3×10^{-7} s and 1×10^{-5} s, the corresponding maximum temperature on the right end are 3,000 and 1,000 K. (c) and (d) show the temperature distribution in Mo SC beam when the maximum temperature at right end are respectively 4,800 K and 1,000 K, the corresponding time (5×10^{-7} s and 2×10^{-6} s) indicates temperature decays more quickly in Mo beam than in Cu–Zr beam. (e) The maximum temperature evolution with time in Cu–Zr and Mo beams. The Mo beam even with larger initial temperature (4,912 K) was quicker to decay to room temperature within 5×10^{-6} s than Cu–Zr beam (3,000 K) within 6×10^{-5} s.

S4 MD simulation of mass transport of Mo single crystal beam

Classical MD code LAMMPS [S9] and visualization code ATOMEYE [S10] were employed in our work. The Molybdenum nanobeam with aspect ratio of 6.5:1 was cut from a rectangular box. $[1\bar{1}\bar{1}]$ direction was chosen to be the uniaxial direction and the other two radial directions are $[0\bar{1}\bar{1}]$ and $[2\bar{1}\bar{1}]$ respectively. F–S potential [S11] was used to describe the atomic interactions. This nanobeam was divided into three large parts: the left dark red part is fixed through the simulation, the middle bright red part is a low temperature region (due to thermal conduction to surroundings in real experiments in Fig. 2) and the rest right part is a high temperature region. For simplicity, the nanobeam was thermally isolated in our MD simulations. In order to characterize the mechanisms of mass transport, the right part was divided into 10 small regions denoted as from R1 to R10 (Fig. S3(a)).

Firstly, by using NVE ensembles, velocities which have a Gaussian distribution at 600 K were assigned to each atom and the beam reached an equilibrium temperature of 441 K after 2 ps. Then the right blue part was heated up to 4,800 K in a very short period of 8 ps, meanwhile, the temperature of the middle part was kept at 441 K but allowing sufficiently large temperature fluctuations. NVT ensembles and Nose-Hoover method were employed during this process. After this heating process, ensemble of the right part was switched to NVE and Nose-Hoover thermostat was turned off. The settings of the middle part were not changed and it is still

allowed to have a temperature fluctuation. From the time-resolved snapshots in Fig. S3(b), the liquid Mo stream shrinks into “mushroom”-like structure driven by surface tension within 80 ps, though the right part was cooled down (still larger than 3,000 K) due to thermal conduction to low temperature region in the middle. And we do not see obvious mass loss because of the evaporation.

Here the square displacement of center of mass of each region is defined as following:

$$\delta_{\text{CM}} = (X_{\text{CM}}(t) - X_{\text{CM}}(0))^2$$

where δ_{cm} is the square displacement of center of mass, $X_{\text{CM}}(t)$ is the center of mass of a specific region at time t , $X_{\text{CM}}(0)$ is the initial center of mass of a specific region. And the mean square displacement of a single atom in each region is calculated by the following equation:

$$\delta_{\text{atom}} = \frac{\sum_1^N (X_i(t) - X_i(0) - X_{\text{CM}}(t) + X_{\text{CM}}(0))^2}{N}$$

where $X_i(t)$ is the atom position at time t , $X_i(0)$ is the initial atom position, N is the atom number in the calculated region. By subtracting the center of mass displacement from the atomic displacement, we get the atomic mean square displacement based on diffusion mechanism. From Figs. S3 (c) and 3(d), we can see that $\delta_{\text{CM}} \gg \delta_{\text{atom}}$ for most of the regions. Therefore, this ultrafast mass transport along the shrinking process is dominated by convection.

S5 Influence of external electrical resistor on the NED

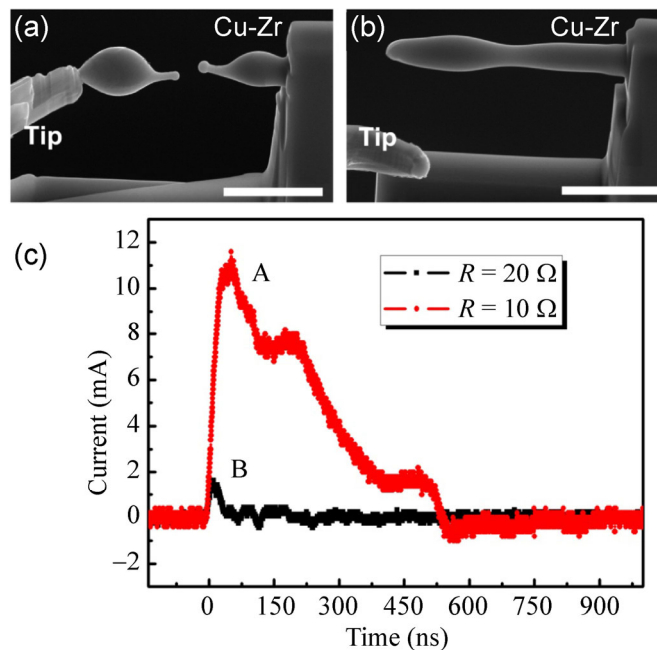


Figure S3 Influence of external resistance R on the MED of Cu–Zr MG beam. (a) and (b) show the formed morphologies of Cu–Zr beams with comparable geometry ($0.9 \mu\text{m} \times 0.9 \mu\text{m} \times 7.5 \mu\text{m}$) after MED when external resistance 10Ω and 20Ω were used in series, respectively. (c) the corresponding electrical pulse current pattern. When the resistance R increased from 10 to 20Ω , the pulse peak decreased by a factor of 5, and the obvious shape evolution was weakened due to the decrease of pulse current. The retained tiny tail in (a) due to Rayleigh instability on the shrunk sphere may indicate the faster diffusion on the surface at high temperature; the melted flow in the core of the beam was arrested by the ensuing rapid cooling. When a smaller electrical pulse was induced, lower temperature was generated by joule heating in the micron-sized beam, then the mass transport driven by surface tension was frozen at a middle state in (b). Scale bar is $3 \mu\text{m}$.

S6 Description of supporting movies and their link addresses

- 1) Movie S1: ED-induced ultrafast mass transport and shape change in a micron-sized refractory Mo beam, forming a “mushroom”-like structure. <http://li.mit.edu/S/ul/Movie/S1.wmv>
- 2) Movie S2: ED-induced ultrafast mass transport and shape change in a micron-sized Cu–Zr metallic glass beam. <http://li.mit.edu/S/ul/Movie/S2.wmv>
- 3) Movie S3: Using MED-induced ultrafast mass transport for high-efficient welding of micron-sized Cu–Zr metallic glass beams. <http://li.mit.edu/S/ul/Movie/S3.wmv>

References

- [S1] Lide, D. R. *Crc handbook of chemistry and physics*; CRC Press, 2009.
- [S2] Jiang, Q. K.; Wang, X. D.; Nie, X. P.; Zhang, G. Q.; Ma, H.; Fecht, H. J.; Bednarcik, J.; Franz, H.; Liu, Y. G.; Cao, Q. P.; Jiang, J. Z. Zr-(cu,ag)-al bulk metallic glasses. *Acta Mater.* **2008**, *56*, 1785–1796.
- [S3] Busch, R.; Kim, Y. J.; Johnson, W. L. Thermodynamics and kinetics of the undercooled liquid and the glass transition of the zr41.2ti13.8cu12.5ni10.0be22.5 alloy. *J. Appl. Phys.* **1995**, *77*, 4039–4043.
- [S4] Ma, D.; Stoica, A. D.; Wang, X. L. Volume conservation in bulk metallic glasses. *Appl. Phys. Lett.* **2007**, *91*.
- [S5] Szofran, F. R.; Gruzalski, G. R.; Weymouth, J. W.; Sellmyer, D. J.; Giessen, B. C. Electronic and magnetic properties of amorphous and crystalline Zr40Cu60-xfex alloys. *Phys. Rev. B* **1976**, *14*, 2160–2170.
- [S6] Nagel, S. R. Temperature dependence of the resistivity in metallic glasses. *Phys. Rev. B* **1977**, *16*, 1694–1698.
- [S7] Johnson, W. L.; Kaltenboeck, G.; Demetriou, M. D.; Schramm, J. P.; Liu, X.; Samwer, K.; Kim, C. P.; Hofmann, D. C. Beating crystallization in glass-forming metals by millisecond heating and processing. *Science* **2011**, *332*, 828–833.
- [S8] Choy, C. L.; Tong, K. W.; Wong, H. K.; Leung, W. P. Thermal conductivity of amorphous alloys above room temperature. *J. Appl. Phys.* **1991**, *70*, 4919–4925.
- [S9] Plimpton, S. Fast parallel algorithms for short-range molecular dynamics. *J. Comput. Phys.* **1995**, *117*, 1–19.
- [S10] Ju, L. Atomeye: An efficient atomistic configuration viewer. *Model. Simul. Mater. Sci. Eng.* **2003**, *11*, 173.
- [S11] Finnis, M. W.; Sinclair, J. E. A simple empirical body potential for transition metals. *Phil. Magaz. A* **1984**, *50*, 45–55.